Mathematical Simulation of Mass Transport in Porous Media: An Innovative Method to Match Geometrical and Transport Parameters for Scale Transition

Journal:	*Drying Technology*
Manuscript ID:	LDRT-2013-0158.R1
Manuscript Type:	General Paper
Date Submitted by the Author:	n/a
Complete List of Authors:	Gavriil, Gavriil; University of Ioannina, Vakouftsi, Eleni; University of Ioannina, Coutelieris, Frank; University of Ioannina, Department of Environmental and Natural Resources Management
Keywords:	Porous media, Transport processes, Modeling, Scale-up, Scale-down

Mathematical Simulation of Mass Transport in Porous Media: An Innovative Method to Match Geometrical and Transport Parameters for Scale Transition

G. Gavriil, E. Vakouftsi & & Frank A. Coutelieris*

Department of Environmental & Natural Resources Management, University of Ioannina

Abstract

The scale-up and scale-down process is of great importance regarding modeling of mass transport phenomena in porous media. Three numerical simulations of porous media for three different scales were developed and validated in this study, analyzing the mass transport phenomena for each scale. More precisely, the first system is a spheres assemblage of various spatial distributions and sizes (mesoscopic), the second is a porous box (macroscopic), and the third is a sphere-in-cell model (microscopic). It was found that the porous structure – shape, size and positioning – of the spheres at the mesoscopic scale have significant effects on the adsorption efficiency (up to 10%) of high convective regimes. It is also concluded that a microscopic description at the pore scale is insufficient to adequately describe mass transport phenomena in porous media due to discontinuities of the structure and high local velocity. By comparing the results from the three scales, we obtained a method of matching all geometrical,

*Corresponding author. Current Address: University of Patras, Seferi 2, 30100, Agrinio, Greece, Tel: +302641074196; Fax: +30 2641074176, fkoutel@cc.uoi.gr

flow and transport parameters when a scale transition occurs. The qualitative description of transport phenomena through the three scales and their identical behavior demonstrates the method's effectiveness.

Keywords: Scale-up, Scale-down, Transport processes, Porous media, Modeling

1. Introduction

Mass transport phenomena in porous media require much research in order to be properly understood due to their potential applications in industry and technology. As porous materials are characterized by high complexity in their invisible internal structure, modeling is a useful tool for understanding transport processes. Computational fluid dynamics (CFD) is the use of computer-based simulation to analyze complex systems involving fluid flow, heat transfer and associated phenomena such as chemical reactions, using mathematical models. The development and application of CFD has recently increased and become a powerful tool in the design and analysis stages of several engineering and industrial systems and processes [1, 2].

When numerical models are used to model field scale flow and transport processes in the subsurface, the problem of scales arises. Typical scales in numerical models, corresponding to spatial resolutions of subsurface heterogeneity, are generally much larger than the measurement scale of the parameters and physical processes involved. The problem is one of assigning parameters at the gridblock scale based on parameter values measured on small scales [3]. The major reason that scale transition must be investigated is to obtain scale dependence of the results occurring by a transport process. It is well established that small-scale heterogeneities can have a significant impact on flow in a porous medium. The applications of fractal geometry to characterize heterogeneities and analyze transport phenomena in porous media have been generally approbatory in many fields [4-6]. However, small-scale heterogeneities cannot be directly incorporated into field-scale simulation models because of limitations in computational

abilities. Therefore, the average effects of small-scale heterogeneities in large-scale numerical grids must be accounted for through the scale-transition process.

The main objective of this study is to develop a new method of scaling-up and/or scaling-down the fundamental processes occurring in a porous medium that can be applied to a wide variety of systems. The focus here is on matching all the geometrical, flow and transport parameters to move from a small-scale model to a full-scale setup and vice versa. To this end, three models, representing three different scales (i.e. micro-, meso- and macro-scale) were studied. In particular, the first model (meso-scale model) was applied to an assemblage of spheres of various sizes and spatial distributions, the second (macro-scale model) to a porous box, and the third (micro-scale model) to a sphere-in-cell geometry. The results were compared and analyzed to obtain a strategy (scale transition rules) towards a globally-valid description to cope with the physicochemical and geometrical characteristics of a porous medium in scale-transition.

2. Problem statement

Consider a porous medium consisting of a solid phase, being distributed within a defined volume of interest and of given specific geometrical characteristics, such as porosity, average pore size, surface over volume ratio, tortuosity, etc. The void space (porous) is occupied by a Newtonian liquid or gas mixture that flows under laminar flow conditions and contains a solute which can react heterogeneously on the solid/liquid or solid/gas interfaces. This reaction process can adequately represent a sorption mechanism under the pressure and temperature conditions specified by the phenomena that take place.

In the present study, a simple, fast hydrocarbon reaction takes place on the catalytic gas/solid interfaces at relatively low temperature. More precisely, the decane oxidization reaction is assumed to occur whenever decane ($C_{10}H_{22}$) and molecular oxygen (O_2) reach the gas/solid interface through advection and/or diffusion. The overall reaction is as follows:

$$C_{10}H_{22}+15.5O_2 \rightarrow 11H_2O+10CO_2 \quad (1)$$

It should be noted that the use of the decane oxidization reaction is optional and any other reaction as well as relative solute could be used in its place.

Since the temperature is fairly low and the oxygen concentration is significantly higher than the decane's, it is reasonable to assume that the reaction rate depends only on the decane's concentration and is of the first order [7-9]. Thus, the reaction rate is given as:

$$r_{C_{10}H_{22}} = -k_c T C_{C_{10}H_{22}} = -k_{c,0} e^{-\frac{E_a}{RT}} C_{C_{10}H_{22}} \quad (2)$$

where k_c is the reaction rate constant, T is the temperature, $C_{C_{10}H_{22}}$ is the decane concentration, E_a is the activation energy, and R is the universal gas constant. For the current simulations, the heterogeneous reaction characteristics were as follows [7]: E_a=226.783 kJ/mole with a pre-exponential factor, $k_{c,0}$=1.66 X 10^{24} m^3/s kg. Furthermore, the reaction temperature varies between 473 K and 483 K approximately, while the inlet composition mixture is presented in Table 1 [7].

The scale of the transport problem could be crucial in obtaining accurate results of macroscopic interest, such as adsorption efficiency. When microscopic geometry is used to model the processes described above, all the local heterogeneities have been taken into account, thus significantly affect the results. As the final results are of macroscopic interest, it is crucial to develop an accurate, general mechanism for scale transition. The present study focuses on the exact matching of geometrical, flow and transport characteristics when scale transition is required. For this reason, a typical porous model of meso-scale is presented, and the results obtained were subsequently scaled-up (macro-scale) and scaled-down (micro-scale).

3. Mesoscopic model

To represent a porous medium in the scale of millimeters, the meso-scale model is created. It is an assemblage of spheres placed in a typical orthogonal box. The spheres represent the solid part of the porous medium and the void space is occupied by the bulk phase. The fluid mixture enters the volume through the inlet surface, reacts on the catalytic layer provided by the solid spheres, and finally exits through the outlet surface (Figure 1). Geometry definition and calculation of the fundamental parameters follow.

The geometry of the 3x2x3 mm meso-scale porous medium is depicted in Figure 1. To exclude end-effects, two extra domains (inlet and outlet) of 1x2x3 mm have been added. These domains allow the flow to deploy before entering the porous volume thus eliminating possible end effects. In Figure 1, the exterior walls of the porous-media volume are hidden so that the assemblage of spheres can be viewed easily. This porous medium corresponds to a typical porosity of 0.7, and sphere radii satisfy normal distribution. Sphere radii and sphere coordinates in the control

volume are calculated by an algorithm implemented in Fortran 90/95 whose steps are described below:

Step (1) Incorporating a random number generator, the position of the sphere's center is generated, always set in a box with specific dimensions (3x2x3 mm).

Step (2) Using a random number generator along with the appropriate routine, a radius is generated, forced to follow a certain distribution (i.e. normal, random or uniform).

Step (3) The void space surrounding each sphere is checked for availability. If it is free (not occupied by another sphere), the radius value is accepted; otherwise step 2 is repeated until an acceptable value is produced.

Step (4) The sphere is posed.

Step (5) Steps 1-4 are repeated until the volume of the positioned spheres satisfies the pre-defined porosity value.

The fundamental transport processes can be described by the following set of conservation equations at steady state [10]. Firstly, the continuity equation may be written as:

$$\nabla \cdot \left(\rho \underline{U} \right) = 0 \qquad (3)$$

where $\underline{U}$ is the velocity vector, and ρ is the fluid density.

Due to the rather low Reynold's numbers, the gas phase flow is considered laminar and can be described by the momentum equation given as:

$$\nabla \cdot \left(\rho \underline{U} \underline{U} \right) = -\nabla P + \nabla \cdot \underline{\underline{\tau}} \tag{4}$$

where P is the pressure and $\underline{\underline{\tau}}$ is the shear stress tensor.

Additionally, heat transfer phenomena described by the energy conservation equation can be expressed as:

$$\nabla \cdot \left(\rho \underline{U} h_i \right) = -\nabla \cdot \underline{q} \tag{5}$$

where h_i is the enthalpy of i-th species (enthalpy of formation and sensible heat), and $\underline{q}$ is the heat flux given by:

$$\underline{q} = -k \nabla T + \sum_{i=1}^{N_g} \underline{J}_i h_i \tag{6}$$

where k is the thermal conductivity (calculated by the kinetic theory of gaseous mixtures [10]), N_g is the total number of gas species, and $\underline{J_i}$ is the mass diffusion flux of the i-th species expressed as:

$$\underline{J_i} = \rho \underline{U} Y_i - \rho D_i \nabla Y_i \tag{7}$$

where Y_i is the i-th species mass fraction, and D_i is the diffusivity of the i-th species in the mixture. Lastly, the species mass fractions are calculated using the mass conservation equation of species:

$$\nabla \cdot \left(\rho \underline{U} Y_i \right) = \nabla \cdot \left(\rho D_i \nabla Y_i \right) + \dot{\omega} \tag{8}$$

where $\dot{\omega}$ is the production/consumption rate of species i due to reactions.

To investigate the performance of the porous medium, the macroscopic adsorption efficiency, λ, is used and it is defined by the ratio of the solute adsorption rate divided by the rate of the upstream influx, and is given by:

$$\lambda = \frac{\iint_{S_{inlet}} \left(C_{C_{10}H_{22}} \underline{U}\right) \underline{n} dS_{inlet} - \iint_{S_{outlet}} \left(C_{C_{10}H_{22}} \underline{U}\right) \underline{n} dS_{outlet}}{\iint_{S_{inlet}} \left(C_{C_{10}H_{22}} \underline{U}\right) \underline{n} dS_{inlet}} \quad (9)$$

where $\iint_{S_{inlet}} (C_{C_{10}H_{22}} \underline{U}) \underline{n} dS_{inlet}$ is the is the total mass flux entering the volume of interest through the inlet surface, S_{inlet} and $\iint_{S_{outlet}} \left(C_{C_{10}H_{22}} \underline{U}\right) \underline{n} dS_{outlet}$ is the is the total mass flux exiting the volume of interest through the outlet surface, S_{outlet} . It should be noted that $\underline{n}$ is the vector normal to each surface.

For their integration, the above equations are generally valid under the following general assumptions. Assuming ideal gases, the mixture density is computed, while the kinetic theory of gases is used for the calculation of viscosity and thermal conductivity [10]. As widely accepted, gravitational effects are neglected and laminar flow is assumed for compressible fluids. The fuel mixture at the entrance is assumed to be homogeneous, considering no mass accumulation either at the entrance or exit. Furthermore, the specific heat is calculated by fittings to experimental Jannaf curves [11]. Stefan-Maxwell equations are employed to calculate the mass diffusion coefficients for multi-component diffusion.

Furthermore, it's worth outlining that non-deformable and non-shrink core model was assumed. Also, given that granular media grains are usually spherical and more scarcely spheroidal [12] in the present model the porous media is assumed to consist of spherical particles [13]. In general, granular media have porosity values higher than 0.8, while porosity approx. 0.45 is the threshold for regular packing. Porosity very close to the packing threshold implies very small pore size and

as a result high Pe numbers are developed locally which is far away from the laminar flow assumption. In the present manuscript, porosity values above 0.6 have been studied.

Regarding the boundary conditions, fixed pressure of 1 atm is applied to the outlet, and normal velocity varying from 10^{-4} to 0.42 m/s is set to the inlet surface, to obtain the wide range of Peclet values considered. The spheres' surfaces are the catalytic layers where decane oxidization occurs. Additionally, a mixture of constant composition enters the system (Table 1) through the entrance surface, and zero mass flux is set to the walls and outlet, assuming zero accumulation. Finally, the inlet mixture is preheated to 473 K and zero heat flux is set to the walls and outlet.

A number of parameters must be defined for the simulations. Given that the sphere radii and their population are known, the porosity, ε, of the mesoscopic geometry is calculated by:

$$\varepsilon = \frac{V_{void}}{V_{total}} = \frac{V_{total} - V_{sph}}{V_{total}} = 1 - \frac{V_{sph}}{V_{total}} \tag{10}$$

where V_{void} represents the void volume of the porous media, V_{total} is the total volume of the medium, and V_{sph} is the volume occupied by the spheres.

Additionally, the tortuosity, τ, of the porous medium, is given by the empirical relation for heterogeneous catalyst as [14]:

$$\tau^2 = \frac{\varepsilon}{1-(1-\varepsilon)^{1/3}} \tag{11}$$

Regarding isothermal conditions, viscosity, μ, is constant, thus permeability, κ, can be calculated using Darcy's law ($u = -\frac{\kappa}{\mu}\nabla P$). For multi-component diffusion, component diffusivities, D_i, are calculated by Stefan-Maxwell equations [15].

The porous media characteristics of the mesoscopic geometries (assemblage of spheres) used in the present simulations are listed in Table 2. It should be mentioned that the average pore size and the surface to volume ratio, S/V, although calculated for the mesoscopic geometries in the present study, are also used for the macro-scale model described in the following section.

Distribution tests were performed to better simulate a real porous medium and examine whether the sphere radii and their location in the porous volume play a crucial role on the solution. As sphere radii are not constant, three different types of distribution (normal, random and uniform) are taken into consideration. Figure 2a depicts the influence of this distribution on adsorption efficiency, as defined by eq (9), for various Peclet numbers, and indicatively for porosity 0.7. It is clearly seen that the different radius distribution does not affect the overall solution for low and moderate Peclet values. However, for relatively high *Pe* values (> 80), a discrepancy can be observed between the curves plotted. This can be attributed to the significant convection being valid for high *Pe*, where the high velocities implied correspond to higher probabilities for the soluble to escape from the porous structure. Under these conditions, radii distribution is crucial because it defines the pore size. Additionally, given that the spheres' radii follow a certain distribution (here, indicatively, the normal distribution), the impact of different sphere placement in the porous volume on λ values is presented in Figure 2b for constant porosity (0.7) and various *Pe* numbers. The results were similar to those seen in Figure 2a. It can be observed that no deviation appears for lower *Pe* numbers, while a small deviation can be seen for higher ones. As a result, since neither the spheres' radii nor their location critically affect the transport processes

when the regime is not strongly convectional, only normal distribution has been considered hereafter.

4. Macroscopic model

To scale-up the mesoscopic model presented above, a macro-scale description was built representing the scale of centimeters. The geometrical characteristics of the macroscopic geometry for ε=0.7, are depicted in Figure 3. Furthermore, similar to the mesoscopic case, the inlet and outlet volume of 10 cm length each, provide the necessary space for the flow to fully develop. At this scale, the porous volume is a box, where the voids and solid spaces have not been geometrically defined in detail. Specifically, it is assumed that both void and solid phases exist everywhere in the porous volume, while all the quantities should be calculated in the sense of spatial-averaging. Therefore, the transport equations and the relative parameters should be modified accordingly.

The partial differential equations previously described in detail apply for the fluid regions (inlet and outlet volumes), while for the porous media volume they are slightly converted as follows.

The mass conservation can be written as:

$$\nabla \cdot \left(\varepsilon \rho \underline{U} \right) = 0 \qquad (12)$$

and flow can be described by:

$$\nabla \cdot \left(\varepsilon \rho \underline{U} \underline{U} \right) = -\varepsilon \nabla P + \nabla \cdot \left(\varepsilon \underline{\underline{\tau}} \right) + \frac{\varepsilon^2 \mu}{\kappa} \underline{U} \tag{13}$$

The heat (energy) transfer is expressed as:

$$\nabla \cdot \left(\varepsilon \rho \underline{U} h \right) = \nabla \cdot \left(k_{eff} \nabla T + \sum_{i=1}^{N_g} \underline{J_i} h_i \right) + \varepsilon \underline{\underline{\tau}} \nabla \underline{U} \tag{14}$$

and the mass conservation equation becomes:

$$\nabla \cdot \left(\varepsilon \rho \underline{U} Y_i \right) = \nabla \cdot \underline{J_i} + \dot{\omega}_i \tag{15}$$

where the mass diffusion flux is expressed as:

$$\underline{J_i} = \rho D_{i,eff} \nabla Y_i \tag{16}$$

The effective diffusion coefficient, $D_{i,eff}$, is calculated by:

$$D_{i,eff} = \varepsilon^{\tau} D_i \quad (17)$$

based on the Bruggeman approach [16] where the porous media is considered a compact bed of spherical particles, while D_i is the mass diffusion coefficient calculated by the Stefan-Maxwell equations.

At this scale, the macroscopic adsorption efficiency is again defined by the ratio of the adsorbed solute divided by the mass entering the volume through the inlet surface, as in eq. (9).

In addition to those mentioned previously, the boundary conditions applied also include the following:

- Flow: Normal velocity varying between 10^{-6} to 0.003 m/s at inlet, fixed pressure of 1 atm to outlet surface, non-slip condition to walls, Darcy's law for porous region.
- Heat transfer: 473K at inlet, zero heat flux ($\underline{n} \cdot \nabla T = 0$) everywhere else.
- Mass transport: Constant fuel mixture at inlet (Table 1), zero mass flux ($\underline{n} \cdot \nabla C_i = 0$) to walls and outlet, decane oxidization on catalytic solid surfaces assuming zero accumulation.

For the macroscopic model, parameters such as porosity, tortuosity and permeability can be defined from the meso-scale solution (Table 2). However, several other parameters that depend on the geometrical scale need to be determined. Prior to analyzing parameter adjustment it is worth mentioning that similar flow characteristics (i.e. *Pe* number) should be preserved to allow the comparison of results between each scale (meso-, macro- and micro-). For the mesoscopic scale, the Peclet number (Pe_{meso}) is given as:

$$Pe_{meso} = \frac{u_{meso} L_{meso}}{D} \tag{18}$$

where u_{meso}, and L_{meso}, are the inlet velocity and characteristic length for the mesoscopic scale, respectively, and D is the diffusion coefficient, calculated by Stefan-Maxwell equations and considered practically constant. Similarly, the *Pe* number for the macroscopic scale (Pe_{macro}) can be computed as:

$$Pe_{macro} = \frac{u_{macro} L_{macro}}{D} \tag{19}$$

To maintain the same flow characteristics, the above dimensional number should be equal, thus:

$$u_{macro} = \frac{u_{meso} L_{meso}}{L_{macro}} \frac{1}{\varepsilon} \tag{20}$$

Given that u_{meso}, L_{meso} and L_{macro} are already known, u_{macro} is easily computed.

Additionally, the average pore size of the macroscopic geometry (a_{macro}) is given by:

$$a_{macro} = \frac{L_{macro}}{L_{meso}} a_{meso} \tag{21}$$

where a_{meso} is the average pore size of the mesoscopic geometry, calculated manually for each case. Specifically, the distance between each two neighboring spheres is measured by subtracting the summation of the two radii from the center-to-center distance. Accordingly, the average value of these results, for all the spheres constituting the porous structure, is the average pore size for each case.

To maintain constant porosity and sphere number during scale-up, the average pore size should be modified proportionally to the rate of upscaling (L_{macro}/L_{meso}), since otherwise it is assumed that the hypothetical spheres in the macroscopic model are squeezed, thus reducing the void space (pores) between them.

The surface to volume ratio, $\left(\frac{S}{V}\right)_{macro}$, can be computed for the macroscopic simulations as:

$$\left(\frac{S}{V}\right)_{macro} = \frac{L_{meso}}{L_{macro}}\left(\frac{S}{V}\right)_{meso} \tag{22}$$

where $\left(\frac{S}{V}\right)_{meso}$ is the surface to volume ratio of the mesoscopic scale considering normal distribution of sphere radii. It is calculated by the summation of the spheres' surface area divided by their volume:

$$\left(\frac{S}{V}\right)_{meso} = \frac{\sum_{i=1}^{n} S_{meso,i}}{\sum_{i=1}^{n} V_{meso,i}} \tag{23}$$

where n is the number of spheres.

To further understand the rule by eq. (22), an indicative example follows in Figure 4. Being non-dimensionless, the surface to volume ratio is affected by the geometrical scale-up. Figure 4a represents a random porous medium in the mesoscopic scale, and Figure 4b depicts the same medium in macroscopic scale. The surface area and volume at the mesoscopic scale are given by:

$$S_{meso} = 4\pi r_{meso}^2 \tag{24a}$$

$$V_{meso} = \frac{4}{3}\pi r_{meso}^3 \tag{24b}$$

Thus,

$$\left(\frac{S}{V}\right)_{meso} = \frac{3}{r_{meso}} \tag{25}$$

Respectively, the surface area and volume at the macroscopic scale are obtained by:

$$S_{macro} = 4\pi r_{macro}^2 \tag{26a}$$

$$V_{macro} = \frac{4}{3}\pi r_{macro}^3 \tag{26b}$$

Thus,

$$\left(\frac{S}{V}\right)_{macro} = \frac{3}{r_{macro}} \tag{27}$$

By dividing the two ratios, it is obtained:

$$\frac{\left(\frac{S}{V}\right)_{macro}}{\left(\frac{S}{V}\right)_{meso}} = \frac{r_{meso}}{r_{macro}} \tag{28}$$

The r_{meso}/r_{macro} ratio is equivalent to the rate of upscaling L_{meso}/L_{macro}, thus eq. (28) becomes eq. (22). All the above transformations compose the transition rule that should be followed to simulate a porous medium in a larger scale.

5. Microscopic model

For the down-scaling process (microscopic scale), the geometry used is a sphere-in-cell (unit cell), consisting of two concentric spheres. The conceptual idea behind this approach is that the unit cell is an adequate representative of the whole medium; therefore, processes occurring through the porous structure are described sufficiently by those occurring in the unit cell. Sphere-in-cell models are based on the representation of the overall solid mass of the swarm by a spherical or cylindrical solid body embedded in a spherical or cylindrical aqueous envelope, respectively. The thickness of the surrounding fluid layer is adjusted so the ratio of the solid volume to the volume of the liquid envelope represents exactly the solid volume fraction of the

porous medium. It should be also mentioned that the unit cell represents the first and simplest model studied in the literature, however, a discontinuity appears at the adjacent inlet and outlet grid cells [17].

In the present study, this model is studied to provide a comparative scale for the outcomes. The geometric characteristics of the microscopic geometry are seen in Figure 5, where typical geometry is presented for porosity 0.7. The outer sphere having 2 mm diameter, represents the control volume. The inner sphere (smaller one) represents the surface (interface) where the heterogeneous catalytic reaction occurs and its diameter is defined by the porosity. The hidden surface on the left is the inlet surface from which the mixture enters the unit cell, and the surface on the right is the outlet surface of the medium.

The transport equations described above were solved for the unit cell taking into account the aforementioned assumptions. Regarding the boundary conditions, the velocity varied from 0.0001 to 0.7 m/s and fixed pressure is applied to the outlet surface. The inner sphere provides the catalytic surface for the oxidization reaction, assuming zero mass flux on the surface. Furthermore, the fuel mixture composition is the same as for the previous cases (see Table 1), and zero mass flux is applied to the outlet. The inlet temperature is set to 473 K, while zero heat flux is set to the outlet.

The porosity of the microscopic geometry is computed by eq (10) preserving the radius of the external sphere constant and modifying the radius of the internal sphere, while tortuosity is given by eq (11). The permeability and diffusivity considering multi-component diffusion is calculated as described previously. The velocity is adjusted accordingly to maintain the Peclet number the same as in the mesoscopic model.

6. Numerics

All the geometries are discretized in space by an unstructured grid, while the macroscopic porous medium, being simpler in terms of geometry creation, is discretized by a non-homogeneously structured grid. To solve the nonlinear strongly coupled conservation equations described previously, the CFD-ACE+ package applying the finite-volume method was adopted and allowed the SIMPLEC (Semi-Implicit Method for Pressure-Linked Equations Consistent) algorithm to calculate the pressure through an iterative procedure. Additionally, only for the mesoscopic geometry in order to determine the sphere radii and the sphere coordinates in the control volume an algorithm was developed in Fortran 90/95 as described in detail in Section 3 Mesoscopic model. For the mathematical calculations, an HP Compaq 6000 Pro MT PC with the following characteristics was used: Intel® Core ™2 Duo CPU E7500 at 2.93GHz and 2GB RAM memory.

Given the required accuracy of at least 10^{-4} for all the involved quantities, the convergence time and the maximum iterations differ for each scale. For the mesoscopic geometry, the convergence time is significantly higher than that of the macroscopic simulations due to its complexity. The convergence time varies between 160 to 300 minutes, while for the macroscopic and microscopic simulations it ranges from 5 to 60 and 10 to 30 minutes, respectively. Additionally, the required iterations for convergence are 300, 2000 and 4000 for the meso-, macro- and macro-scopic simulations, respectively.

Finally, to ensure that the simulation outcomes are not affected by the discretization used, grid independency tests were conducted for each scale. For the mesoscopic geometry the number of unstructured cells increased from 59700 to 299000 approximately and by increasing further from 210700 cells the adsorption efficiency values affected only by 0.03%, while the convergence

time tripled. For the macroscopic case the node points in x, y and z directions increased creating 20700 to 130000 cells and increase above 35100 cells changed λ only by 0.4% and extended convergence time by 250%. For the microscopic geometry the number of cells varied between 46000 and 217000 and refining further the grid (more than 110000 cells) affects λ by 0.8%. Thus, based on the above the number of cells used was 210700 for the meso-, 35100 for the macro-, and 110000 for the micro-scale geometry.

7. Validation

Unfortunately, at this point it should be noted that neither experimental nor theoretical results on decane oxidation in porous materials are available for a direct comparison of the simulation results and only a qualitative validation could be conducted. Specifically, the comparison of simulation results was made against the experimental results published in [18] and used for validation purposes in papers regarding simulation of mass transport in porous structures [19, 13]. These comparison results are depicted in Figure 6a and 6b for the unit cell model and the case of sphere assemblage, respectively.

In each case, it can be observed that the qualitative behavior of the adsorption efficiency is in good accordance with the existing literature. The fairly high discrepancy in terms of quantitative comparison observed in all scales, can be attributed to the different characteristic of the porous media considered such as tortuosity as well as to the different surface reactions and/or sorption mechanisms considered in these works. Finally, it should be stress out that the results for macroscopic scale are directly compared with those for mesoscopic one, since no experimental or theoretical data for macroscopic transport in porous structures with porosity between 0.6 and 0.9 are available in the relative literature.

8. Results & Discussion

The mass fraction of oxidized decane is presented in Figure 7 for all scales. As mentioned previously, to compare the results, the simulations were carried out keeping both porosity and Peclet number constant (porosity = 0.7 and Pe=50) for all scales. It is clearly presented in Figure 7 that the mass fraction gradients are towards the solid mass, wherever it has been explicitly defined, i.e. mesoscopic (Figure 7a) and microscopic (Figure 7b) scale, and it is proportional to the flow for the macroscopic case (Figure 7c) where the exact location of the solid phase is uncertain. Furthermore, decane consumption increases slightly with scale since the available adsorbing mass also increases with scale. Constant porosity ensures that the solid volume fraction is the same in all cases, however the adsorbing surface (i.e. the adsorbing mass itself) is not the same and follows the S/V trend.

Furthermore, for porosity =0.7 and Pe=50 the temperature variation along the flow direction is depicted in Figure 8a for meso-scale and in Figure 8b for macroscale, while the temperature spatial distribution in the unit cell volume can be seen is Figure 8c. The exothermic decane oxidization reaction increases the temperature in the flow direction as decane is consumed (Figure 7). Particularly, for the meso-scale case, the temperature obtains higher values locally i.e on the catalytic surface, an effect that could not be seen in the macroscale geometry due to the space-averaged approach and quantities used. It should be mentioned that the exact positions of the spheres (i.e. the solid phase) in the porous volume is not geometrically defined in the macroscopic scale. However, the difference between the absolute maximum temperature and the absolute minimum in all cases is too low (approximately 5-12 degrees) to have a significant effect on the physical parameters (diffusivity, permeability, thermal conductivity etc.).

The adsorption efficiency, λ, as a function of the Peclet number is depicted for various porosities in Figures 9-11. Figure 9 represents the mesoscopic geometry, Figure 10 the macroscopic geometry, and Figure 11 the microscopic geometry. It can be observed that for all porosities and all geometrical scales, adsorption efficiency decreases with Peclet number, since the flow becomes more convective and as a result the species are forced to exit the porous media before participating in the oxidization reaction. For low *Pe* numbers, the diffusion regime dominates the convective one. This allows the reactant species to approach the catalytic surface where the reaction occurs and to equalize the concentration of the reacted species (Fick's law). It is worth noting that for a high reaction rate constant such as the one used in the present simulations, λ reaches the maximum value of approx. 100%. The effect of porosity on λ values is also presented in these figures. In Figure 9, the adsorption efficiency in general decreases as porosity increases, except of some minor discrepancies (<10%) for specific porosity values, that can be attributed to the stochastic character of the assemblage's structure (spheres locations and radii, etc) as well as to the accuracy numerically obtained. From physical point of view, as porosity values become higher, the void volume within the medium increases and consequently, the solid volume, which provides the catalytic surface for the heterogeneous reaction of decane oxidation [eq. (1)], decreases, leading to lower λ values. This behavior has also been widely reported elsewhere (see, for example [13, 19]). Regarding the macroscopic case, Figure 10 shows the same general behavior of λ with Pe and ε. An overlap of the ε=0.7 and ε=0.8 curves is observed, which can be attributed to the empirical relation given by eq. (11), which is used to compute tortuosity, as well as to the calculation of the geometry's characteristics (i.e. porosity, average pore size, permeability and surface to volume ratio).

Finally, the effect of *Pe* and porosity on the adsorption efficiency for microscopic (sphere-in-cell) geometry is shown in Figure 11. It is noteworthy that for *Pe*>50 approximately the sphere-in-cell is insufficient to adequately describe such physicochemical problems, since the adsorption efficiency increases with porosity, although the opposite phenomenon is expected. This behavior can be attributed to the high local velocities located in the contact area of the inlet boundary condition with the outlet boundary condition (i.e., at the area of the two - inlet and outlet - adjacent boundary cells). The high local velocity is an indigenous, conceptual weakness of the unit cell approach, because the unit cell concept, as presented by Kuwabara [20], is neither space filling, nor energy conservative and does not take into account the interference of other grains, etc. All these shortcomings lead to high local advection causing gradient to the species mass fraction (Figure 12). As a result, the sphere-in-cell geometry will no longer be used in the present study because the other two geometries are more efficient and accurate. Future proposals will not be made for the correction of the microscopic geometry, since present technology allows for the numerical solution of more detailed models and provides accurate results.

Applying the scale transition rule presented previously, Figure 13 presents the comparison between mesoscopic and macroscopic geometry for different *Pe* numbers and porosities varying between 0.6-0.9. It can be seen that the adsorption efficiency decreases with Peclet and with the porosity for all the cases. For low Peclet numbers where the regime is mainly diffusive, the mesoscopic and macroscopic models predict almost the same λ, presenting a maximum discrepancy of 4%. The higher difference between these two geometries for intermediate and high *Pe* values (50<*Pe*<100) can be attributed to the more detailed consideration that takes place in the case of the mesoscopic geometry. Furthermore, it can be observed that decane consumption slightly increases with the scale, since the available adsorbing mass also increases

with the scale. Constant porosity ensures that the solid volume is the same in all cases, however, the adsorbing surface (i.e. the adsorbing mass itself) is not the same and follows the S/V trend.

9. Conclusions

The transport phenomena taking place in porous media were studied to develop a fast and easy method of estimating macroscopic quantities (such as adsorption efficiency) during scale transition from mesoscopic to macroscopic (scale-up) or to microscopic (scale-down) geometries. The fundamental transport processes (laminar flow, convection, diffusion and heterogeneous reaction) were described in detail for each scale used. It was found that as *Pe* increases, adsorption efficiency values become lower for all scales. However, in the case of the unit cell, this behavior was only noticed for relatively low to medium *Pe* numbers (Pe<50). For high *Pe* numbers, the velocity reaches high values at the point where the inlet surface meets the outlet surface, thus leading to discontinuity. Therefore, it was proved that sphere-in-cell geometry is insufficient to simulate mass transport phenomena for high Peclet numbers. Furthermore, it was found for all scales that, as the porosity value decreases, λ increases, because the catalytic surface where the oxidization reaction takes place also increases.

A method of matching parameters when scale transition occurs was proposed, underlying the necessary steps that should be followed. The three scales were compared for different *Pe* numbers and by varying the porosity from 0.6 to 0.9. It was observed that for the low and high *Pe* numbers used in this study, the curves of mesoscopic and macroscopic geometry overlap, thus proving that there is no need to analytically simulate porous media, a procedure that is time consuming both in terms of creating the involved geometry and acquiring the solution through

the iterative process. However, the deviations recorded for medium *Pe* numbers make the proposed methodology sufficient only for low to moderate Peclet values.

10. References

[1] Rizzi, A.; Nørstrud, H.; Siikonen, T.; CFD Developments in the Northern European Countries. In 100 Volumes of Notes on Numerical Fluid Mechanics; Egon, H.H., Ernst, K., Eds.; Springer: Berlin, 2009; 133-140.

[2] Brenner, G.; CFD in Process Engineering. In 100 Volumes of Notes on Numerical Fluid Mechanics; Egon, H.H., Ernst, K., Eds.; Springer: Berlin, 2009; 341-349.

[3] Liu, H.H.; Bodvarsson, G.S. Upscaling of constitutive relations in unsaturated heterogeneous tuff matrix. Journal of Hydrology 2003, 276, 198-209.

[4] Cai, J.; Yu, B.; Zou, M.; Luo, L. Fractal characterization of spontaneous Co-current imbibition in porous media. Energy fuels 2010, 24, 1860–1867.

[5] Kerdpiboon, S.; Devahastin, S. Fractal Characterization of Some Physical Properties of a Food Product under Various Drying Conditions. Drying Technology 2007, 25, 135–146.

[6] Cai J.; Yu, B. A Discussion of the Effect of Tortuosity on the Capillary Imbibition in Porous Media. Transport of Porous Media 2011, 89, 251–263.

[7] Caravella, A.; Hara, S.; Hara, N.; Obuchi, A.; Uchisawa, J. Computational Fluid Dynamics Simulation of a Three-Dimensional Catalytic Layer for Decane Oxidation: Case Study Reaction on Particle Surface. Industrial Engineering Chemical Research 2011, 50, 11879-11888.

[8] Battin-Leclerc, F.; Fournet, R.; Glaude, P.A.; Judenherc, B.; Warth, V.; Come, G.M.; Scacchi, G. Modeling of the gas-phase oxidation of n-decane from 550 to 1600 K. Proceedings of the Combustion Institute 2000, 28, 1597–1605.

[9] Atkins, P.; Paula J.D. Physical Chemistry (9th Ed.); W.H. Freeman and Company: NewYork, 2010.

[10] Bird, R.B.; Stewart, W.; Lightfoot, E.N. Transport Phenomena (2nd Ed.); John Wiley & Sons Inc.: New York, 1960.

[11] Goos, E.; Burcat, A.; Ruscic, B. Extended Third Millennium Ideal Gas and Condensed Phase Thermochemical Database for Combustion with updates from Active Thermochemical Tables; U.S. Department of Energy: Tennessee, 2011.

[12] Coutelieris, F.A. The influence of axial orientation of spheroidal particles on the adsorption rate in granular porous medium. Studies in Surface Science and Catalysis 2002, 144, 745-751.

[13] Coutelieris, F.A., Kainourgiakis, M.E., Stubos, A.K. Low to moderate Peclet mass transport in assemblages of spherical particles for a realistic adsorption–reaction–desorption mechanism Powder Technology 2005, 159, 173–179.

[14] Shen, L.; Chen, Z. Critical review of the impact of tortuosity on diffusion. Chemical Engineering Science 2007, 62, 3748–3755.

[15] Runstedtler, A. On the modified Stefan–Maxwell equation for isothermal multicomponent gaseous diffusion. Chemical Engineering Science 2006, 61, 5021–5029.

[16] Pulkrabek, W.W. Engineering fundamentals of the internal combustion engine (2nd Ed.); Pearson Prentice Hall: USA, 2003.

[17] Guo, G.; Thompson, E. Experimental analysis of local mass transfer in packed beds. Chemical Engineering Science 2001, 56, 121–132.

[18] Wilson, E.J.; Geankoplis, C.J. Liquid Mass Transfer at Very Low Reynolds Numbers in Packed Beds. Industrial & Engineering Chemistry Fundamentals 1966, 5, 9-14.

[19] Coutelieris, F.A.; Kainourgiakis M.E.; Stubos, A.K. Low Peclet Mass Transport in Assemblages of Spherical Particles for two different adsorption mechanisms. Journal of Colloid & Interface Science 2003, 264, 20-29.

[20] Kuwabara, S. The forces experienced by randomly distributed parallel circular cylinder or spheres in a viscous flow at small Reynolds numbers. Journal of Physical Society of Japan. 1959, 3, 527–531.

11. Nomenclature

Latin letters

C_i Concentration of the i-th species [mol m^{-3}]

D_i Diffusivity of i-th species in the mixture [m^2s^{-1}]

E_a Activation energy [$Jmol^{-1}$]

h_i Enthalpy of the i-th species [Jkg^{-1}]

J_i Mass diffusion flux of the i-th species [$kgm^{-2}s^{-1}$]

k Thermal conductivity [$Wm^{-1}K^{-1}$]

k_c Reaction rate constant [$m^3s^{-1}kg^{-1}$]

$k_{c,0}$ Pre-exponential factor [$m^3s^{-1}kg^{-1}$]

L Characteristic length [m]

$\underline{n}$ Vector normal to the surface [-]

n Number of spheres [-]

N_g Total number of gas phase species [-]

P Pressure [atm]

Pe Peclet number [-]

$\underline{q}$ Heat flux [$Jm^{-2}s^{-1}$]

r_i Reaction rate of i-th species oxidization [mol kgs^{-1}]

R Universal gas constant, 8.314 [$Jmol^{-1}K^{-1}$]

r Radius of sphere [m]

S Surface [m^2]

T Temperature [K]

$\underline{U}$ Velocity vector [ms^{-1}]

u Velocity [ms^{-1}]

V Volume [m^3]

Y_i Mass fraction of i-th species [-]

Greek letters

α Average pore size [m]

ε Porosity [-]

κ Permeability [m^2]

λ Adsorption efficiency [-]

μ Viscosity [$kgm^{-1}s^{-1}$]

ρ Density [kgm^{-3}]

$\underline{\underline{\tau}}$ Shear stress tensor [Nm^{-2}]

τ Tortuosity [-]

$\dot{\omega}$ Production/consumption rate of species in the mixture [mol $m^{-3}s^{-1}$]

Subscripts

eff Effective [-]

i Index [-]

inlet Inlet surface [-]

macro Macroscopic [-]

meso Mesoscopic [-]

micro Microscopic [-]

outlet Outlet surface [-]

sph Spheres [-]

void Void space [-]

Figures Captions

Figure 1. Mesoscopic geometry (porosity=0.7, normal distribution).

Figure 2. Geometry dependence tests: (a) distribution, (b) placement (ε=0.7).

Figure 3. Macroscopic geometry (ε= 0.7).

Figure 4. Porous medium in: a) mesoscopic, and b) macroscopic scale.

Figure 5. Microscopic geometry for porosity 0.7.

Figure 6. Validation of (a) microscopic and (b) mesoscopic scale results with experimental data presented in [18].

Figure 7. Mass fraction for (a) mesoscopic, (b) microscopic, and (c) macroscopic scale (porosity=0.7, Pe=50).

Figure 8. Temperature variation of the (a) mesoscopic, (b) macroscopic, and (c) microscopic geometry (porosity=0.7, Pe=50).

Figure 9. Adsorption efficiency of the mesoscopic geometry as a function of Pe for various ε.

Figure 10. Adsorption efficiency of the macroscopic geometry as a function of Pe for various ε.

Figure 11. Adsorption efficiency of the microscopic geometry as a function of Pe for various ε.

Figure 12. Discontinuities in the flow field for the microscopic geometry.

Figure 13. Comparison between mesoscopic and macroscopic geometry for various Peclet numbers and porosities.

Tables captions

Table 1. Inlet fuel mixture composition.

Table 2. Geometrical characteristics for mesoscopic porous medium (normal distribution).

Table 1. Inlet fuel mixture composition

Species	$C_{10}H_{22}$	CO_2	O_2	H_2O	NO	N_2	Total
Mass Fraction	0.0002	-	0.05	0.1	0.0002	0.8496	1.0

Table 2. Geometrical characteristics for mesoscopic porous medium (normal distribution)

Porosity [-]	0.6	0.7	0.8	0.9
Permeability [m^2]	8.91E-10	8.23E-10	7.40E-10	3.01 E-10
Tortuosity [-]	1.50	1.45	1.38	1.30
Average pore size [m]	0.00027	0.00038	0.00036	0.00083
S/V [m^{-1}]	8874.31	8594.38	8244.43	7822.89

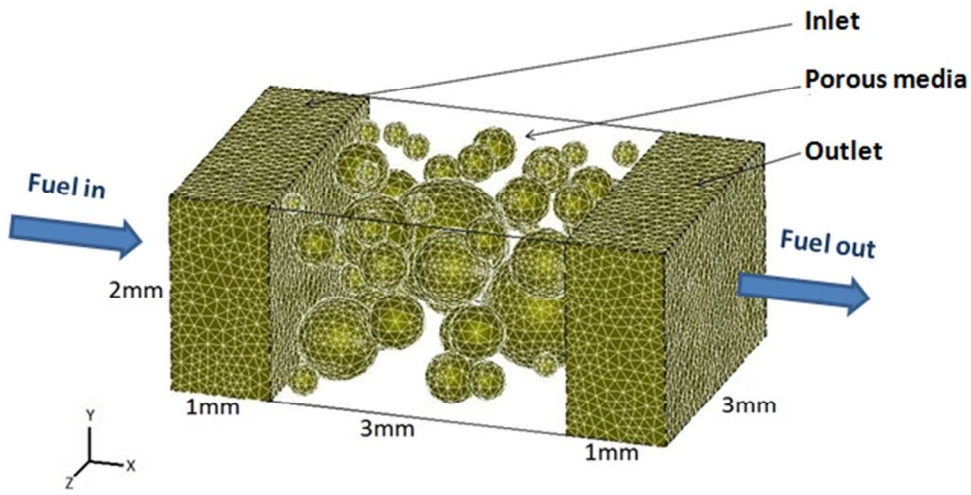

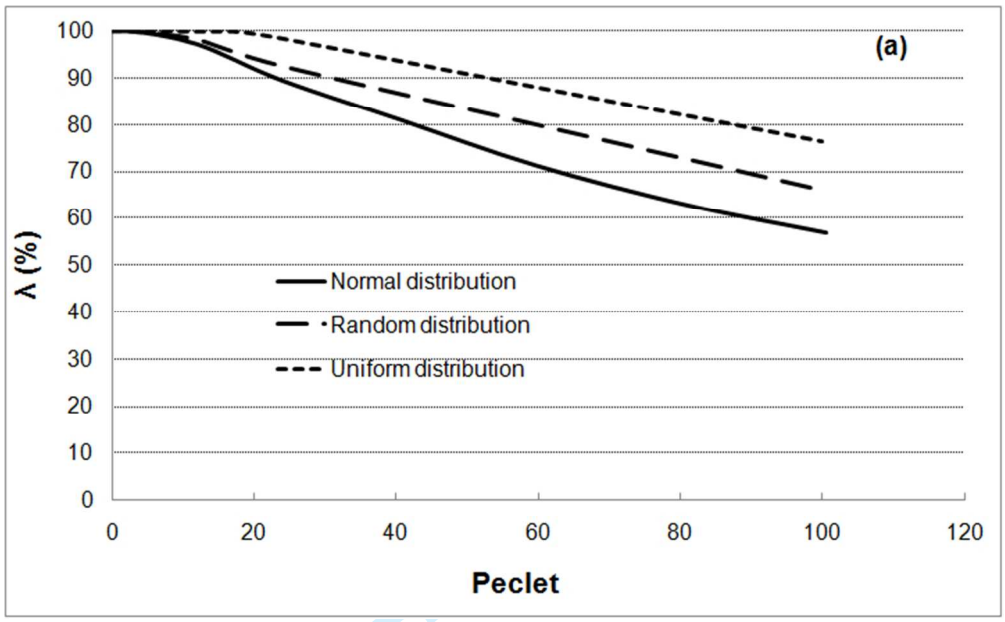

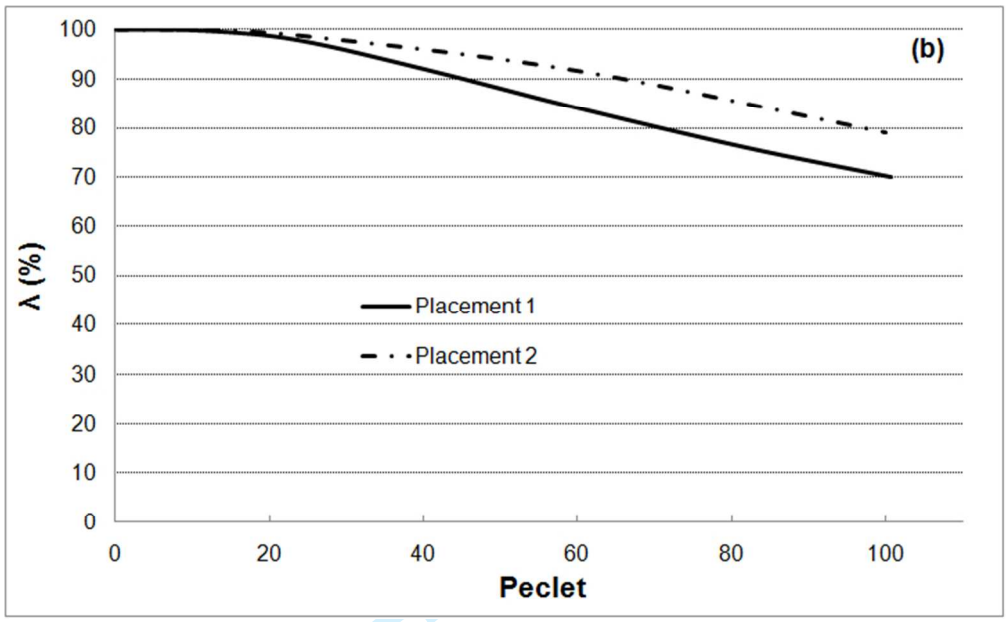

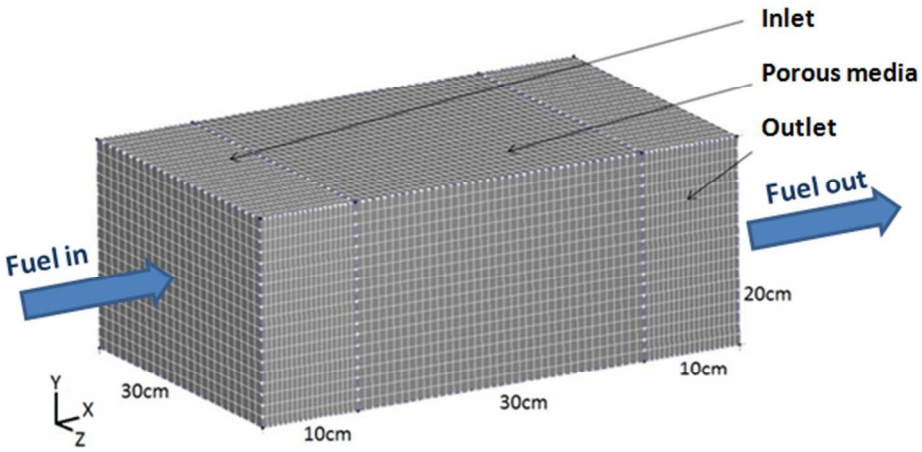

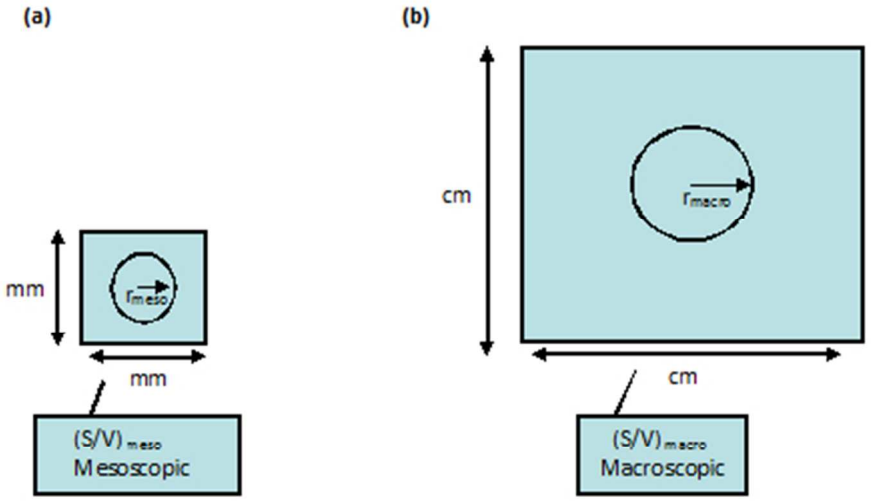

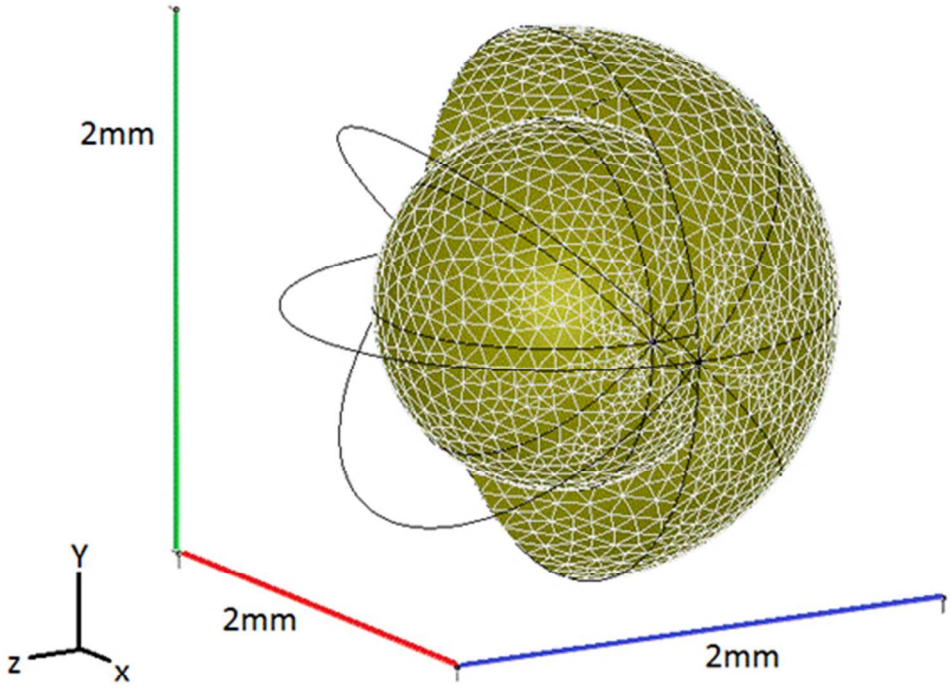

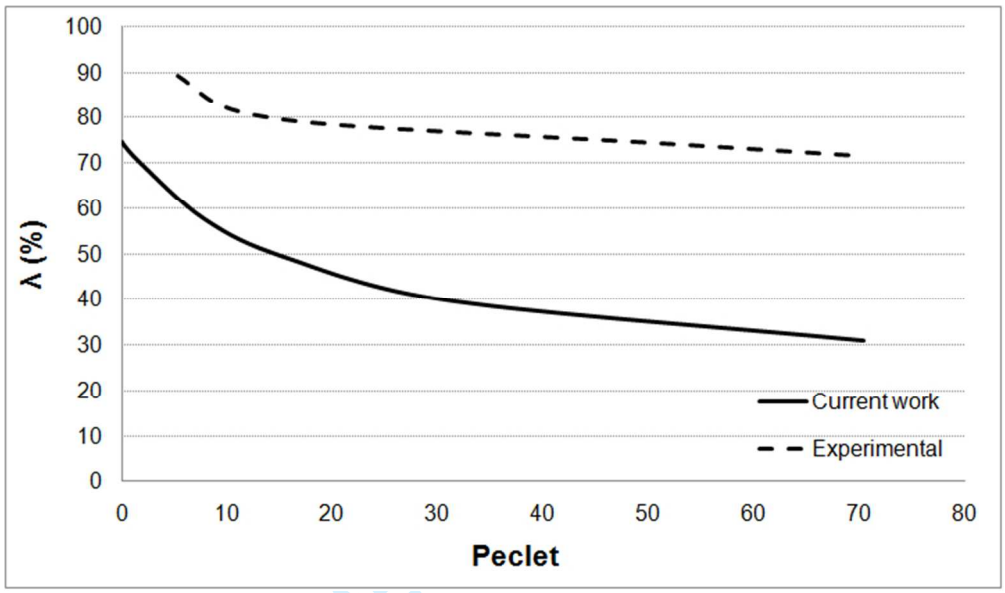

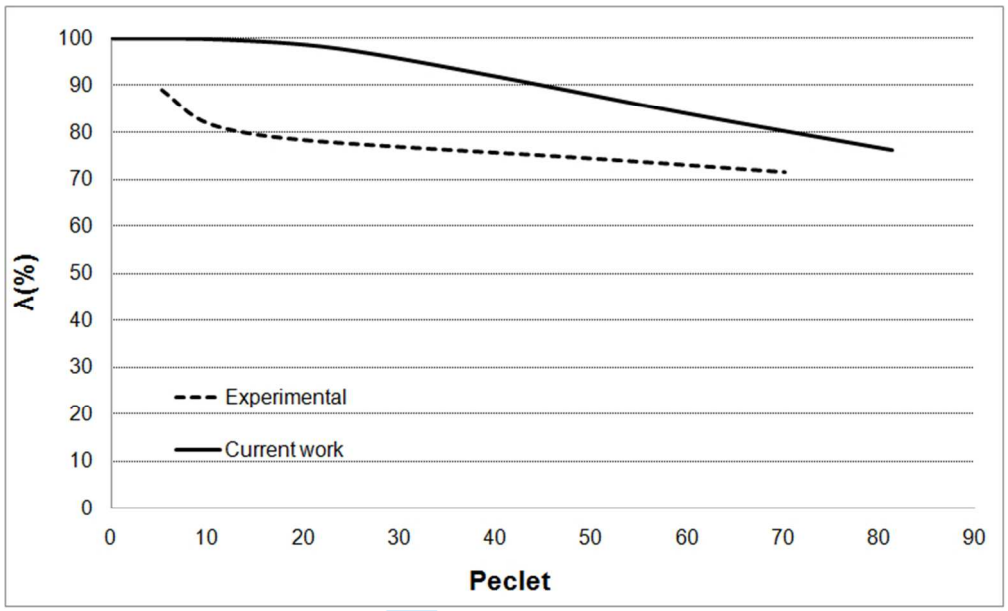

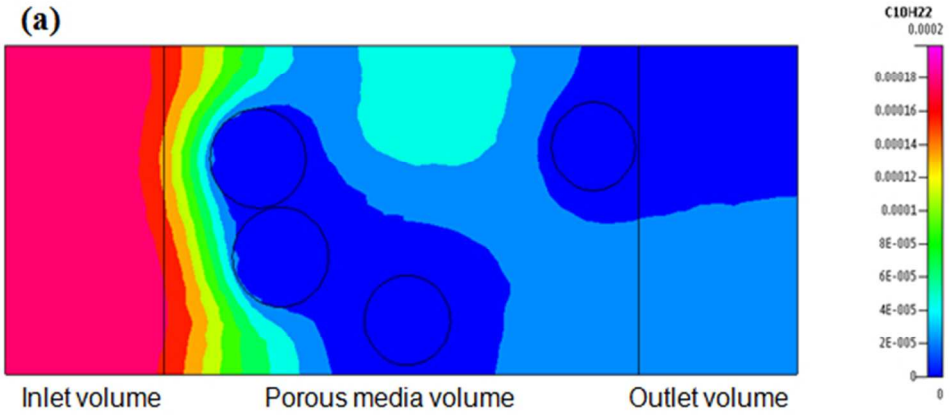

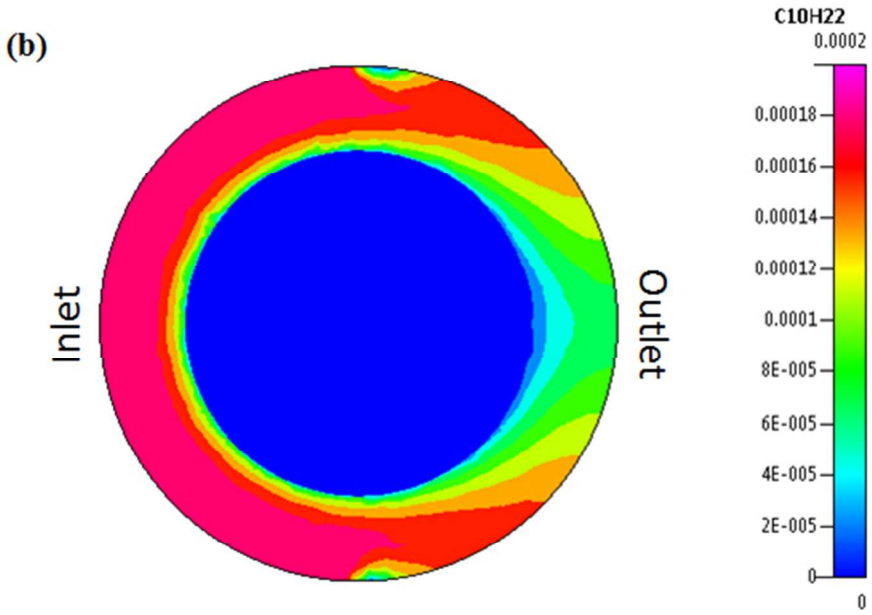
(b)
Inlet
Outlet
C10H22
0.0002
0.00018
0.00016
0.00014
0.00012
0.0001
8E-005
6E-005
4E-005
2E-005
0
0

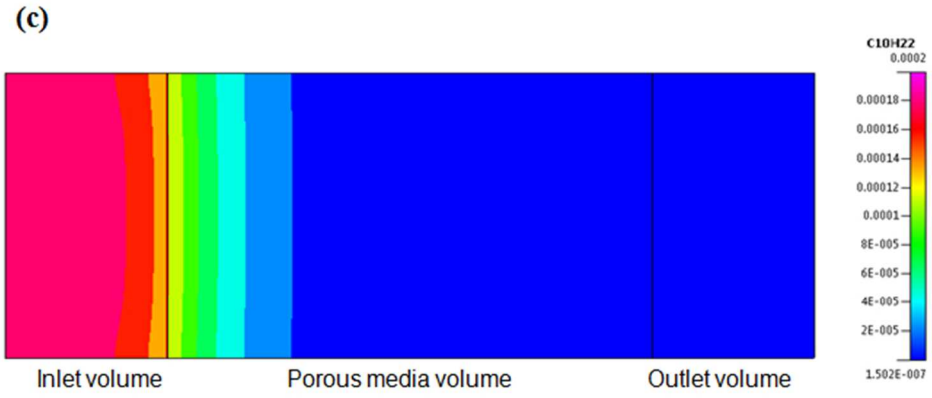

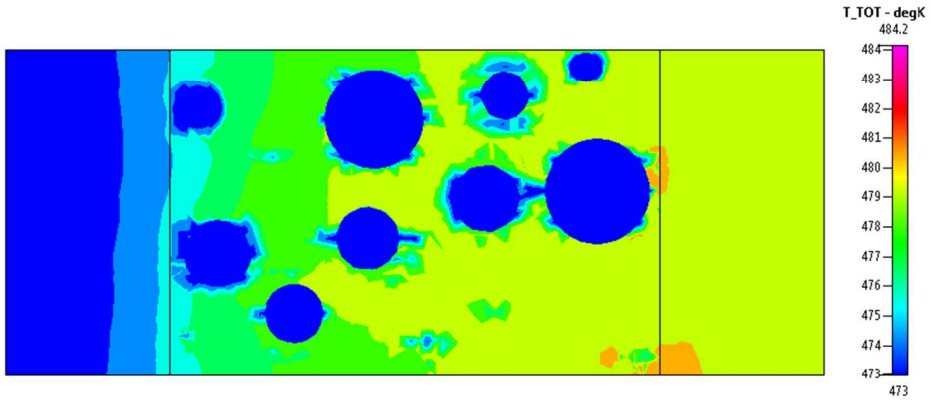

(a)

312x151mm (74 x 74 DPI)

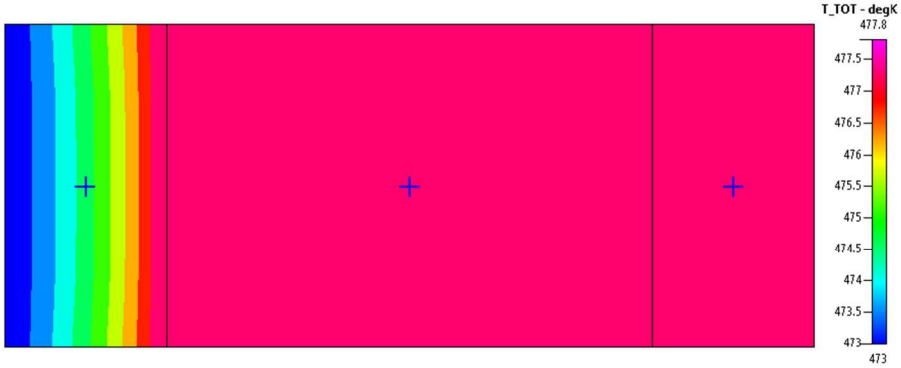

(b)

337x152mm (74 x 74 DPI)

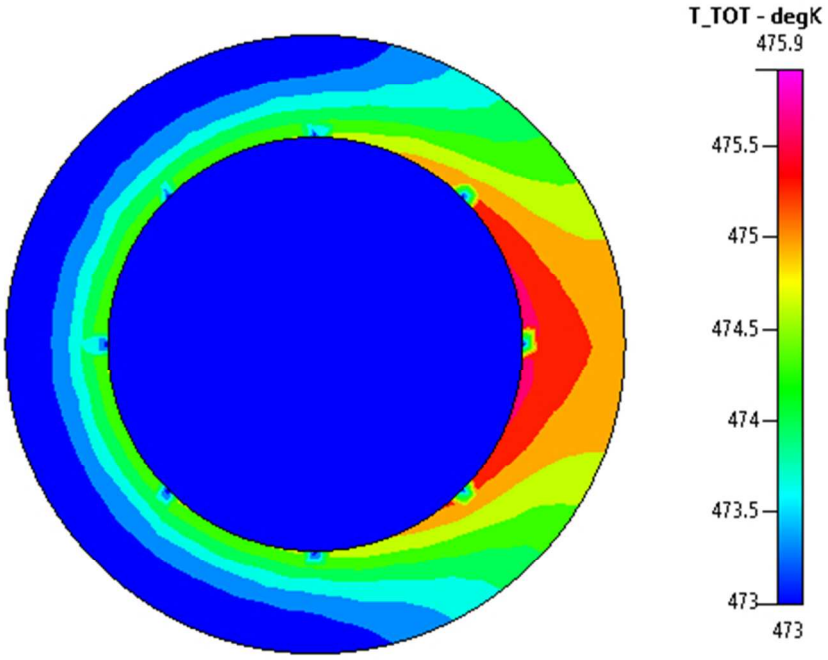

(c)

192x146mm (74 x 74 DPI)